RSC Advances

PAPER

View Article Online
View Journal | View Issue

Cite this: *RSC Adv.*, 2014, **4**, 4831

In_2O_3 nanoplates: preparation, characterization and gas sensing properties

Xiumei Xu,[a] Xin Li,[a] Wenbo Wang,[a] Biao Wang,[b] Peng Sun,[a] Yanfeng Sun*[a] and Geyu Lu*[a]

Received 28th August 2013
Accepted 14th October 2013

DOI: 10.1039/c3ra44708a

www.rsc.org/advances

In this work, a simple route for the synthesis of irregular In_2O_3 nanoplates in the presence of oleic acid and urea is described. The structure and morphology of the as-obtained product were characterized using X-ray powder diffraction (XRD), field emission scanning electron microscopy (FESEM) and transmission electron microscopy (TEM). The results indicate that the synthesized In_2O_3 nanostructures are composed of irregular nanoplates. The gas sensing properties of the as-obtained product were investigated. The sensor based on the In_2O_3 irregular nanoplates exhibits a remarkably enhanced response and a fast response/recovery time towards NO_2.

1. Introduction

With the increasing concerns on air pollution and human health and safety, the need for high sensitive gas sensors has increased. For the purpose of effectively detecting toxic and hazardous gases, significant efforts have been focused on exploring new materials with enhanced gas-sensing performances.[1–4] The detection of NO_2 is important for monitoring environmental pollution resulting from combustion or automotive emissions. Existing gas sensor materials include semiconducting metal oxides,[5] silicon[6,7] and organic materials.[8,9] Semiconducting metal oxides such as WO_3 and SnO_2 have been widely used[10] for NO_2 detection. The wide variety of functional materials with hierarchical structures have provided plenty of opportunities for exploring novel properties and superior device performances due to their dramatically increased surface area, great level of crystallinity, and the possible complete depletion of carriers within the nanostructure when exposed to the target gas. Hence, over the past decade, many research groups have focused on controlling the morphology of inorganic nanostructures.[11–14] Generally, the working mechanism of semiconductor gas sensors lies in changes in the sensor resistance resulting from surface effects.

As a very important wide-band-gap (direct band gap around 3.6 eV) n-type semiconductor, In_2O_3 has been recognized as a promising semiconductor material for gas sensors, window heaters, solar cells and liquid-crystal displays[15–21] due to its non-toxicity and excellent stability. Due to the high conductivity and abundant defects both in the sensing body and on the surface, indium oxide (In_2O_3) is a promising candidate for practical applications. Especially, In_2O_3 has shown a superior response and selectivity towards detecting NO_2 gas, while it is not very sensitive to reducing gases.[22] Through structure design, the sensing properties of semiconductor oxides can be greatly improved, especially for detecting low concentrations of NO_2 (ppb level). In order to improve the performance of devices based on In_2O_3, various morphologies of In_2O_3 with different dimensional nanostructures, such as porous nanosheets,[23] nanopyramids and nanocolumns,[24] nanofibers,[25] nanorods,[26] nanotubes,[27] nanowires,[28] and complex hierarchical structures,[29] have been synthesized *via* a series of routes. These nanostructures provide good building blocks for the development of high performance gas sensors.

Herein, we report a facile method for the preparation of In_2O_3 irregular nanoplates by a simple process. The gas-sensing properties of the as-obtained In_2O_3 product were also investigated. The sensor based on the as-obtained irregular In_2O_3 nanoplates exhibited a superior sensing performance towards low NO_2 concentrations at relatively low operating temperatures.

2. Experimental

2.1. Synthesis and characterization of the In_2O_3 nanoplates

All the reagents (analytical-grade purity) were used without any further purification. In a typical synthesis, 0.381 g of $In(NO_3)_3 \cdot 4.5H_2O$ and 0.25 mL oleic acid were added to 36 mL of water to form a mixed solution at room temperature. Then, 0.3 g of urea was added into the above mixed solution under vigorous stirring. After being alternately stirred and ultrasonically treated, the mixture solution was transferred to a 40 mL

[a]*State Key Laboratory on Integrated Optoelectronics, College of Electronic Science and Engineering, Jilin University, 2699 Qianjin Street, Changchun 130012, People's Republic of China. E-mail: alugy@jlu.edu.cn; Fax: +86 431 85167808; Tel: +86 431 85167808*

[b]*State Key Laboratory of Luminescence and Application, Changchun Institute of Optics, Fine Mechanics and Physics, Chinese Academy of Sciences, Changchun 130033, People's Republic of China*

teflon-lined stainless steel autoclave, sealed tightly, and maintained at 120 °C for 12 h. After the autoclave had naturally cooled to room temperature, the precipitate was washed with deionized water and absolute ethanol several times using a centrifuge, and then dried at 80 °C for 1 day. The precipitate was loaded into an alumina boat, which was placed in a furnace. The samples were calcined at 500 °C for 2 h with a heating rate of 2 °C min^{-1}. The calcined product was then collected for further analysis.

X-ray power diffraction (XRD) analysis was conducted on a Rigaku D/max-2500 X-ray diffractometer with CuKα1 radiation ($\lambda = 1.54056$ Å) in the range of 20–70°. The mean crystallite size was calculated using the Debye–Scherrer formula, $D = 0.89\lambda/(\beta \cos \theta)$, where λ is the X-ray wavelength, θ is the Bragg diffraction angle and β is the peak width at half maximum. The specific surface area was estimated using the Brunauer–Emmett–Teller (BET) equation based on the nitrogen adsorption isotherm obtained with a Micromeritics Gemini VII apparatus (Surface Area and Porosity System). The samples were degassed under vacuum at 200 °C for 4 h prior to the measurements. The pore size distribution was determined using the Barrett–Joyner–Halenda (BJH) method applied to the desorption part of the adsorption–desorption isotherm. Field emission scanning electron microscopy (FESEM) images were recorded on a JEOL JSM-7500F microscope operating at 15 kV. Transmission electron microscopy (TEM), selected-area electron diffraction (SAED), and high-resolution transmission electron microscopy (HRTEM) images were obtained on a JEOL JEM-2100 microscope operated at 200 kV.

2.2. Fabrication and performance of the sensor

The gas sensor was fabricated as follows: the as-obtained powder was mixed with deionized water in order to make a paste, which was applied on an alumina tube (4 mm in length, 1.2 mm in external diameter, and 0.8 mm in internal diameter, attached to a pair of gold electrodes) by a small brush to form a thick coating film. The thickness of the sensing film was about 100 μm. After drying at room temperature for 30 min, the sensing device was sintered at 500 °C for 2 h. A pair of gold electrodes were installed at each end of the ceramic tube before it was coated with the paste, and each electrode was connected to two Pt wires. A Ni–Cr heating wire was inserted in the tube to form an indirectly-heated gas sensor. The structure of the sensor is shown in Fig. 1.

The electrical properties of the sensor were measured by an RQ-2 series Intelligent Test Meter (China). The response of the sensor was defined as $S = R_g/R_a$ for an oxidizing gas or R_a/R_g for a reducing gas, here, R_a and R_g are the resistance of the sensor in air and the target gas, respectively. The response time was defined as the time required for the variation in the resistance to reach 90% of the equilibrium value after a test gas was injected, and the recovery time was the time necessary for the sensor to return to 10% above the original resistance in air after releasing the test gas.

3. Results and discussion

3.1. Structural and morphological characteristics of the as-obtained In_2O_3

X-ray powder diffraction (XRD) analysis was performed to investigate the crystal phases of the $In(OH)_3$ precursor prepared by the hydrothermal method and the In_2O_3 product obtained by calcining the $In(OH)_3$ precursor.

It can be seen from Fig. 2a that all the diffraction peaks can be indexed to standard cubic $In(OH)_3$, which is consistent with the standard data file (JCPDS file no. 73-1810). After calcination at 500 °C, the $In(OH)_3$ precursor was converted into the pure cubic structure of In_2O_3 according to JCPDS file no. 06-416, with the space group $Ia\bar{3}$ (no. 206) and the lattice parameter $a = 10.118$ Å. No diffraction peaks from any other impurities were observed, indicating the high purity of the products. The mean crystallite size of In_2O_3 was calculated to be around 15 nm using the Debye–Scherrer formula.

The morphology of the samples was investigated by field emission scanning electron microscopy (FESEM). Fig. 3 shows the typical FESEM images of the sample at different magnifications. The low magnification FESEM images (Fig. 3a–c) clearly show that the product is composed of irregular nanoplates. No other morphologies can be observed, indicating the high uniformity of the as-obtained products. As can be seen from

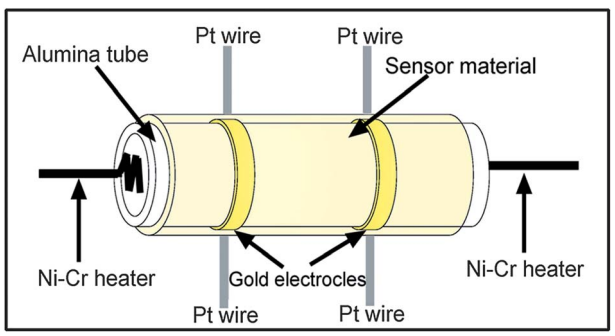

Fig. 1 Schematic structure of the gas sensor.

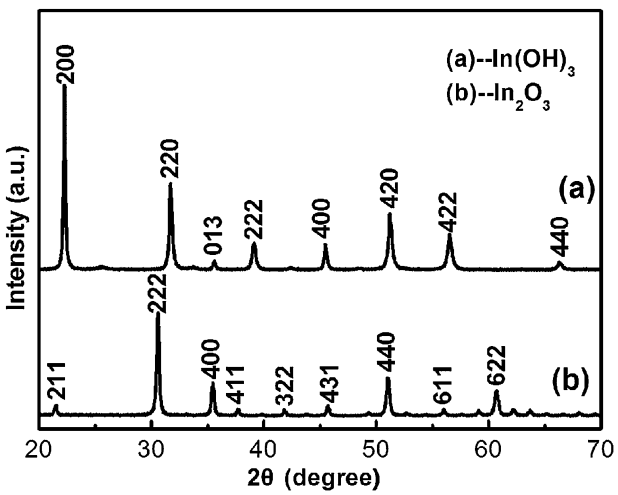

Fig. 2 X-ray diffraction patterns of the as-prepared samples.

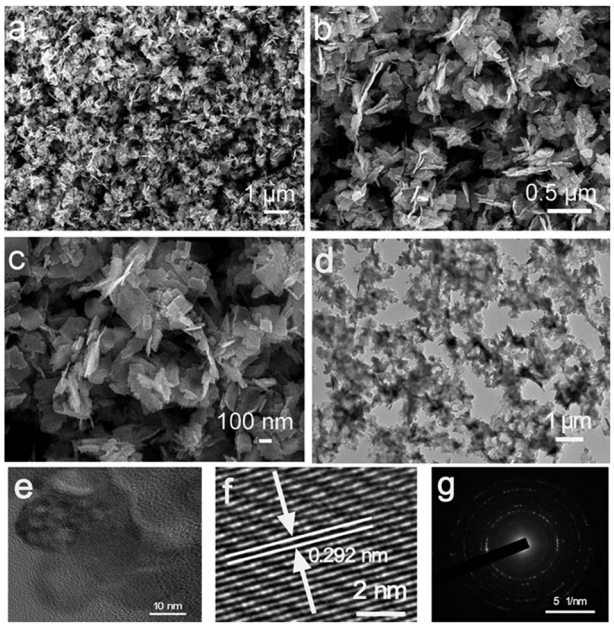

Fig. 3 FESEM images of the as-synthesized In_2O_3: (a) a panoramic and (b) a magnification. (c) A high-magnification FESEM image of the In_2O_3 nanoplates. (d and e) Typical TEM images of the In_2O_3 nanostructures. (f) HRTEM image taken from (d and e). (g) The corresponding SAED pattern.

Fig. 3d and e, irregular nanoplate nanostructures were obtained, which is in agreement with the SEM results, and each nanoplate is composed of several crystallites with a size of about 15 nm. The high-resolution transmission electron microscopy (HRTEM) image (Fig. 3f) shows the fringe distance of 0.292 nm corresponding to the lattice distance of the (222) plane of cubic In_2O_3. The corresponding SAED pattern of a single nanoplate (Fig. 3g) confirms that the In_2O_3 nanoplates are polycrystalline structures in nature.

To obtain further structure information about the as-obtained In_2O_3, the nitrogen adsorption and desorption isotherm was measured at 77 K. The representative N_2 adsorption and desorption isotherm and the corresponding BJH pore size distribution plot (inset) of the nanoplates are shown in Fig. 4. The BET surface area of the product was calculated to be 38.9 $m^2 g^{-1}$ using the Brunauer–Emmett–Teller (BET) method. The pore size distribution curve was calculated from the desorption part of the nitrogen isotherm by the BJH method using the Halsey equation.

3.2. Gas-sensing properties for NO_2

The correlation between the response and the response time of the sensor based on the In_2O_3 nanoplates towards 1 ppm NO_2 at different operating temperatures were measured and are shown in Fig. 5. It was found that the response time decreases with the increasing operating temperature. For the sensor using the In_2O_3 nanoplates, the response to 1 ppm NO_2 increases when the operating temperature rises from 100 to 150 °C, and then gradually decreases. This tendency indicates that a fast response can be obtained by increasing the operating temperature. However, when the operating temperature is too high, the gas response decreases sharply. This decrease in the response at high temperatures may be attributed to the decrease in the number of active sites for the adsorption of NO_2. Since at high temperatures large amounts of oxygen molecules dissociate and are adsorbed on the active sites, the number of free active sites for the adsorption of NO_2 molecules is dramatically reduced and so is the response to NO_2. Another possibility is that at such high temperatures, the rate of adsorption is lower than that of desorption.[15–17] Accordingly, considering those two aspects, the large gas response and the fast response of the sensor towards 1 ppm NO_2, the optimum operating temperature for the sensor using the as-obtained In_2O_3 was determined to be 150 °C, which was hereinafter applied in all the investigations. The effect of the humidity was also investigated at a working temperature of 150 °C. According to the experimental results (not shown here),

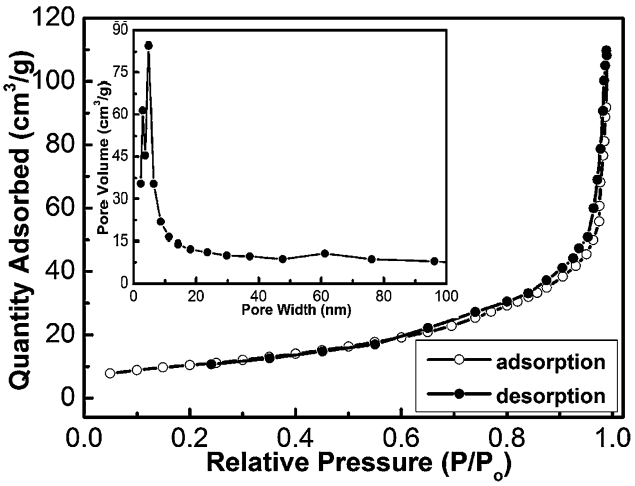

Fig. 4 Typical N_2 adsorption–desorption isotherm of the In_2O_3 nanoplates. The inset is the corresponding pore size distribution curve.

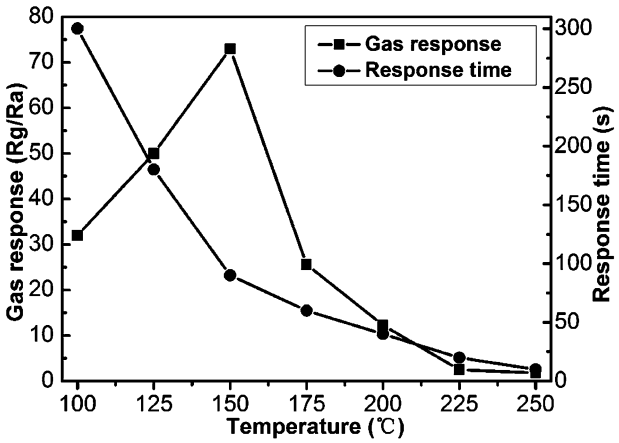

Fig. 5 Correlation between the gas response and the response time towards 1 ppm NO_2 and the operating temperature for the sensor using the as-obtained In_2O_3.

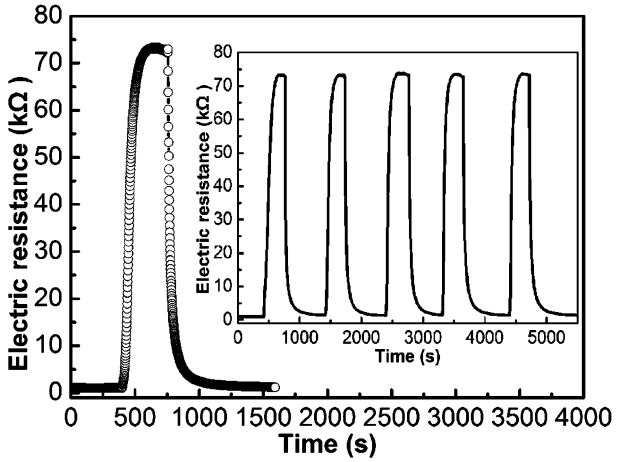

Fig. 6 Response transients of the sensor towards 1 ppm NO_2 at 150 °C, the inset displays the response curves of five cycles.

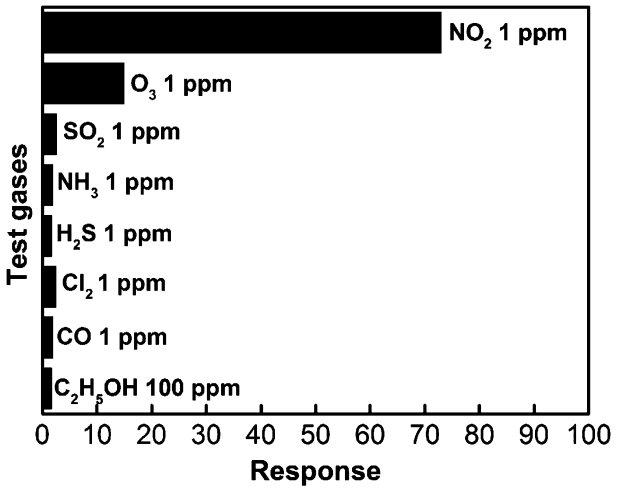

Fig. 8 Cross-responses of the sensor to various test gases at 150 °C.

humidity has no obvious effects on the gas response. Similar phenomena have also been demonstrated in the literature.[30–32]

The response transients of the In_2O_3 nanoplate sensor towards 1 ppm NO_2 was measured at 150 °C (Fig. 6), the response time and recovery time were found to be about 90 s and 40 s, respectively. The response curves of five reversible cycles indicated a stable and reproducible response, as shown in the inset of Fig. 6. It can be observed that the average response was 73 towards 1 ppm NO_2. The dynamic response resistance of the sensor based on the In_2O_3 nanoplates (Fig. 7) to different NO_2 concentrations was investigated at 150 °C. The resistance of the sensor increased upon exposure to NO_2, and decreased in the absence of NO_2. Furthermore, the response of the sensor to NO_2 increased with the increasing NO_2 concentration. The sensor can detect 500 ppb NO_2, and the response is 34. The responses to 1.0, 1.5, 2.0, 2.5, 3.0, 3.5, 4.0, 4.5 and 5.0 ppm NO_2 were about 73, 118, 152, 182, 197, 233, 274, 306 and 344, respectively. Selectivity is an important parameter for a gas sensor. Fig. 8 shows the cross-sensitivities of the In_2O_3 nanoplate sensor to various gases, including O_3, NH_3, CO, H_2S, SO_2, Cl_2, and C_2H_5OH. It is clear that the In_2O_3 sensor exhibits the largest response towards NO_2 among the tested gases. Such a result indicates that the In_2O_3 nanostructure sensor exhibits an excellent selectivity towards NO_2 against the other tested gases at the working temperature of 150 °C.

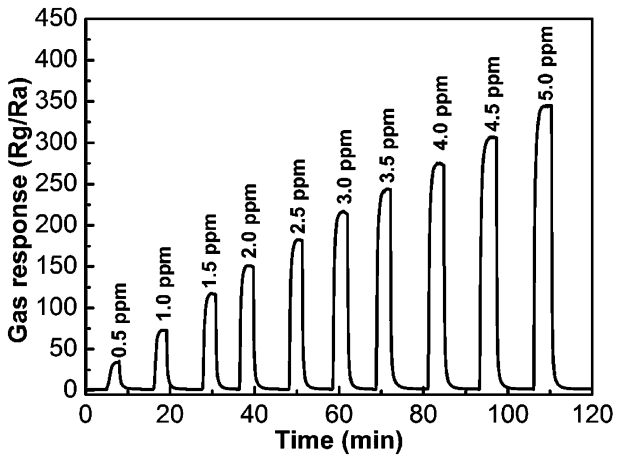

Fig. 7 Response of the sensor using In_2O_3 towards different concentrations of NO_2 at 150 °C in the range of 0.5–5 ppm.

4. Conclusion

In summary, In_2O_3 nanoplates have been successfully synthesized through a simple one-step solution route combined with a subsequent calcination process. Field emission scanning electron microscopy and transmission electron microscopy results demonstrated that the product is composed of nanoplates. The gas sensing properties towards NO_2 of the sensor based on the as-synthesized In_2O_3 were investigated. The sensor fabricated from these nanostructures exhibits excellent NO_2 sensing properties at relatively low operating temperatures. The sensing response is about 34 towards 500 ppb NO_2 at 150 °C. These results suggest that our sensor might have potential application in the fabrication of NO_2 gas sensor devices.

Acknowledgements

This work was supported by the National Nature Science Foundation of China (no. 61074172, 61134010 and 61006055), the Application and Basic Research of Jilin Province (20130102010JC), the China Ministry of Public Security (no. 2011ZDYJJLST010), the Program for Chang Jiang Scholars and Innovative Research Team in University (no. IRT1017) and the "863" High Technology Project (2013AA030902).

References

1 K. Wetchakun, T. Samerjai, N. Tamaekong, C. Liewhiran, C. Siriwong, V. Kruefu, A. Wisitsoraat, A. Tuantranont and S. Phanichphant, *Sens. Actuators, B*, 2011, **160**, 580–591.

2 X. J. Huang and Y. K. Choi, *Sens. Actuators, B*, 2007, **122**, 659–671.
3 A. Gurlo, *Nanoscale*, 2011, **3**, 154–165.
4 E. Comini, C. Baratto, G. Faglia, M. Ferroni, A. Vomiero and G. Sberveglieri, *Prog. Mater. Sci.*, 2009, **54**, 1–67.
5 Y. Shimizu and M. Egashira, *MRS Bull.*, 1999, **24**, 18–24.
6 H. M. McConnell, *Science*, 1992, **257**, 1906–1912.
7 C. Christofides, *Physics, Devices*, Wiley, New York, 1993.
8 J. Miasik, A. Hooper and B. Tofield, *J. Chem. Soc., Faraday Trans. 1*, 1986, **82**, 1117–1126.
9 S. Capone, S. Mongelli, R. Rella and P. Siciliano, *Langmuir*, 1999, **15**, 1748–1753.
10 (*a*) J. Zhang, S. Wang, Y. Wang, Y. Wang, B. Zhu, H. Xia, X. Guo, S. Zhang, W. Huang and S. Wu, *Sens. Actuators, B*, 2009, **135**, 610–617; (*b*) B. Cao, J. Chen, X. Tang and W. Zhou, *J. Mater. Chem.*, 2009, **19**, 2323–2327.
11 J. Zeng, M. Hu, W. Wang, H. Chen and Y. Qin, *Sens. Actuators, B*, 2012, **161**, 447–452.
12 H. Zheng, J. Z. Ou, M. S. Strano, R. B. Kaner, A. Mitchell and K. Kalantar-zadeh, *Adv. Funct. Mater.*, 2011, **21**, 2175–2196.
13 E. Comini, *Anal. Chim. Acta*, 2006, **568**, 28–40; S. Agarwala, Z. H. Lim, E. Nicholson and G. W. Ho, *Nanoscale*, 2012, **4**, 194–205.
14 Y. Bi, D. Li and H. Nie, *Mater. Chem. Phys.*, 2010, **123**, 225–230.
15 G. Korotcenkova, A. Cerneavschia, V. Brinzaria, A. Vasilieva, M. Ivanova, A. Cornetb, J. Moranteb, A. Cabotb and J. Arbiolb, *Sens. Actuators, B*, 2004, **99**, 297–303.
16 J. Tamaki, C. Naruo, Y. Yamamoto and M. Matsuoka, *Sens. Actuators, B*, 2002, **83**, 190–194.
17 T. Hyodo, H. Inoue, H. Motomur, K. Matsuo, T. Hashishin, J. Tamaki, Y. Shimizu and M. Egashira, *Sens. Actuators, B*, 2010, **151**, 265–273.
18 D. H. Zhang, C. Li, S. Han, X. L. Liu, T. Tang, W. Jin and C. W. Zhou, *Appl. Phys. Lett.*, 2003, **82**, 112–114.
19 C. G. Granqvist, *Appl. Phys. A: Solids Surf.*, 1993, **57**, 19–24.
20 Y. Shigesato, S. Takaki and T. Haranoh, *J. Appl. Phys.*, 1992, **71**, 3356–3364.
21 A. Gurlo, M. Ivanovskaya, N. Bârsan, M. Schweizer-Berberich, U. Weimar, W. Göpel and A. Diéguez, *Sens. Actuators, B*, 1997, **44**, 327–333.
22 M. Ivanovskaya, A. Gurlo and P. Bogdanov, *Sens. Actuators, B*, 2001, **77**, 264–267.
23 X. M. Xu, D. W. Wang, W. B. Wang, P. Sun, J. Ma, X. H. Liang, Y. F. Sun, Y. G. Ma and G. Y. Lu, *Sens. Actuators, B*, 2012, **171–172**, 1066–1072.
24 P. Guha, S. Kar and S. Chaudhuri, *Appl. Phys. Lett.*, 2004, **85**, 3851–3853.
25 C. H. Liang, G. W. Meng, Y. Lei, F. Phillipp and L. D. Zhang, *Adv. Mater.*, 2001, **13**, 1330–1333.
26 Z. X. Cheng, X. B. Dong, Q. Y. Pan, J. C. Zhang and X. W. Dong, *Mater. Lett.*, 2006, **60**, 3137–3140.
27 X. P. Shen, H. J. Liu, X. Fan, Y. Jiang and J. M. Hong, *J. Cryst. Growth*, 2005, **276**, 471–477.
28 Y. F. Hao, G. W. Meng, C. H. Ye and L. D. Zhang, *Cryst. Growth Des.*, 2005, **5**, 1617–1621.
29 C. Q. Wang, D. Chen, X. L. Jiao and C. L. Chen, *J. Phys. Chem. C*, 2007, **111**, 13398–13403.
30 N. Matsunaga, G. Sakai, K. Shimanoe and N. Yamazoe, *Sens. Actuators, B*, 2003, **96**, 226–233.
31 A. Dieguez, A. Romano-Rodriguez, J. R. Morante, J. Kappler, N. Barsan and W. Gopel, *Sens. Actuators, B*, 1999, **60**, 125–137.
32 T. K. H. Starke, G. S. V. Coles and H. Ferkel, *Sens. Actuators, B*, 2002, **85**, 239–245.